Showcasing research from Prof. Xiaojing Hao's laboratory, University of New South Wales, Sydney, Australia.

A non-destructive UV Raman characterisation platform to enable insight into the mechanism of reversible ultraviolet-induced degradation (UVID) in TOPCon solar cells

Scientia Prof. Xiaojing Hao's research group at UNSW Sydney focus on developing efficient, durable, and cost-effective solar PV technologies. In this work, they addressed the challenge of widely concerned UV-induced degradation (UVID) in Si solar cells by developing a novel characterisation platform. Their non-destructive characterisation can *in situ* monitor the microscopic material transformations during the UVID and recovery process, effectively unveiling the underlying mechanism of the reversible UVID in Si solar cells. This work provides guidance for the development of international testing protocols and supports the creation of effective UVID-mitigating strategies.

Image reproduced by permission of Caixia Li from *Energy Environ. Sci.*, 2026, **19**, 1148.

As featured in:

See Ziheng Liu, Xiaojing Hao *et al.*, *Energy Environ. Sci.*, 2026, **19**, 1148.

ROYAL SOCIETY OF CHEMISTRY

rsc.li/ees

Registered charity number: 207890

Energy & Environmental Science

ROYAL SOCIETY OF CHEMISTRY

PAPER

View Article Online
View Journal | View Issue

Cite this: *Energy Environ. Sci.*, 2026, **19**, 1148

A non-destructive UV Raman characterisation platform to enable insight into the mechanism of reversible ultraviolet-induced degradation (UVID) in TOPCon solar cells

Pengfei Zhang, †[a] Caixia Li,†[a] Ziheng Liu,†*[a] Jialiang Huang,[a] Jialin Cong,[a] Jingwen Cao,[a] Kun Yu,[b] Jing Zhou,[b] Liyan Miao,[b] Jingming Zheng,[b] Tingting Li,[b] Jie Yang,[b] Wusong Tao,[b] Xinyu Zhang,[b] Hao Jin,[b] Minglei Sun,[c] Jefferson Zhe Liu, [c] Su-huai Wei,[d] Martin A. Green[a] and Xiaojing Hao*[a]

Ultraviolet light-induced degradation (UVID) has been reported across mainstream high-efficiency Silicon (Si) solar cell architectures, including heterojunction (HJT), passivated emitter and rear cell (PERC) and tunnel oxide passivated contact (TOPCon) solar cells, causing up to 10% efficiency loss after continuous exposure to high UV doses. Encouragingly, this degradation has also been reported to be recoverable under certain conditions, such as light soaking. However, in the absence of a clear mechanistic understanding of both the degradation and recovery process, current testing protocols and stability metrics fall short of capturing the true UV resilience of these devices. Establishing a fundamental understanding of UVID is therefore critical for developing more predictive testing frameworks and durable cell architectures under real-world operating conditions. In this work, we demonstrate that the UVID of TOPCon silicon solar cells can be effectively recovered using light soaking in the first place. The recoverable macroscopic cell performance is subsequently found correlated with two reversible changes at the materials level: front surface reflectance by optical transmission of SiN_x and a Boron-doped Si Raman peak by UV Raman spectroscopy. With further atom probe tomography (APT) investigation and theoretical modeling, the mechanisms of this reversible UVID and light soaking induced recovery (LSIR) process are identified. The elucidation of the reversible UVID mechanism at the atomic level directly informs the development of effective mitigation strategies. We demonstrate that the synchronous use of a thick AlO_x film and a low Si : N ratio SiN_x layer can improve the UVID resistance of TOPCon solar cells. Moreover, the non-destructive material level characterisation platform established in this work enables effective capture of the degree of UVID resistance in the design of durable TOPCon solar cells with the potential of in-line quality control.

Received 28th August 2025,
Accepted 2nd January 2026

DOI: 10.1039/d5ee05078b

rsc.li/ees

Broader context

As the global demand for renewable energy accelerates, silicon-based solar cells remain at the forefront of photovoltaic technologies due to their high efficiency and cost-effectiveness. However, long-term reliability and durability under real-world conditions are critical factors that directly impact their performance and commercial viability. One emerging challenge is ultraviolet light-induced degradation (UVID), which has been observed across various high-efficiency silicon solar cell architectures and attracted world-wide attentions. This degradation can lead to remarkable efficiency losses (up to 10%) over time, potentially undermining the gains made through advanced cell designs. Despite reports of partial recovery through light soaking, the lack of a clear mechanistic understanding of UVID and its reversibility has hindered the development of robust testing protocols and effective mitigation strategies. Addressing this knowledge gap is essential not only for enhancing the stability of current solar cell technologies but also for informing the design of future generations of durable and UV-resilient photovoltaic devices.

[a] *School of Photovoltaics and Renewable Energy Engineering, The University of New South Wales (UNSW), Sydney, NSW 2052, Australia. E-mail: xj.hao@unsw.edu.au, ziheng.liu@unsw.edu.au*
[b] *Zhejiang Jinko Solar Co., Ltd, Jiaxing, Zhejiang Province 314416, China*
[c] *Department of Mechanical Engineering, The University of Melbourne, Parkville, VIC 3010, Australia*
[d] *Eastern Institute of Technology, Ningbo, Zhejiang Province 315200, China*
† These authors contribute equally to this work.

Introduction

Ultraviolet light exposure is an inevitable stress factor for outdoor photovoltaic modules, yet its long-term impact on device reliability remains inadequately addressed. Ultraviolet light-induced degradation (UVID) of varying severity has been reported in a series of mainstream high-efficiency silicon (Si) solar cell structures, including heterojunction (HJT), passivated emitter and rear cell (PERC), and tunnel oxide passivated contact (TOPCon), resulting in efficiency losses of up to 10%.[1–8] Meanwhile, UVID has been shown to be recoverable under certain conditions, such as light soaking, electron injection, and annealing at elevated temperatures.[3,6,8] Although UVID is attracting significantly increasing interest during the last two years, most of these studies have primarily focused on macroscopic performance changes in the tested cells or modules, lacking a clear mechanistic understanding of UVID and its recovery process. Thus, the absence of the fundamental understanding of the reversible UVID hinders the development of appropriate accelerated testing protocols that reflect real-world operating conditions and limits progress in formulating effective mitigation strategies.

The reported UVID effects vary significantly with cell architecture and the materials used.[5,9] For example, UVID of HJT solar cells is primarily attributed to the breaking of silicon–hydrogen (Si–H) bonds in the amorphous Si layer, and a process associated with the well-established Staebler–Wronski effect is proposed.[1,10,11] UVID in HJT cells has also been partially recovered by light soaking, however, the underlying mechanism has not yet been fully understood.[6]

On the other hand, UVID of TOPCon cells, which are projected to be the dominant silicon cell technology in the next decade according to the International Technology Roadmap for Photovoltaics,[12] has been investigated even less than that of HJT cells. Instead of relying on hydrogen-rich amorphous silicon layers, TOPCon cells utilise polycrystalline Si layers and thin oxide layers, such as silicon oxide (SiO_x) and aluminum oxide (AlO_x), to achieve good surface passivation.[8,13–15] In TOPCon cells, hydrogen is primarily incorporated within silicon nitride (SiN_x) layers, which serve as anti-reflective coatings (ARC) rather than the primary passivation layer. This distinction makes the UVID mechanisms in TOPCon cells more complex and even less understood compared to HJT cells.

Nevertheless, the UVID phenomena of TOPCon cells have drawn increasing attention recently, and relative investigations have been carried out using UV exposure tests.[3,4,8] Unfortunately, the mechanism for UVID in TOPCon cells is still far from clear since most of the current research still focuses on examining the change in macroscopic cell performance caused by the reproduced UVID process and lacks characterisation from the material level. Even though in some studies, UVID has been correlated to certain fabrication procedures, such as the layer thickness of AlO_x,[8] the core material-level process of UVID is still unclear.

To better reveal the root cause of reversible UVID process in TOPCon cells, in this work, we employed a comprehensive suite of characterisation techniques to directly link macroscopic cell performance degradation to microscopic material transformations. Particularly, we utilised 325 nm UV Raman spectroscopy, which is sensitive to the changes at the very top layers. Besides characterising the already degraded TOPCon cell, an ultra-fast *in situ* examination protocol was also developed to directly characterise the TOPCon cells under UV radiation. The *in situ* monitoring of the UVID and the following recovery process offers an efficient approach to reveal the underlying mechanisms. Moreover, this ultra-fast *in situ* examination method can also be used to diagnose whether a TOPCon cell is vulnerable to UVID in seconds compared to the traditional UVID test that may take days or even weeks, providing fast feedback for process optimisation and the potential for in-line quality control.

In the following sections, we firstly demonstrate that the UVID of TOPCon solar cells can be effectively recovered using light soaking. Furthermore, two reversible changes at the material-level are identified during the UVID and subsequent light soaking induced recovery (LSIR), namely transformation in front surface reflectance and the Si Raman peak. Based on these observations, a possible mechanism for the reversible UVID process is proposed, which is further verified by atomic level atom probe tomography (APT) and theoretical modeling. Additionally, the developed non-destructive characterisation platform is also utilised to prove the effectiveness of high UVID-resistance strategies.

Results and discussions

The *I–V* performance of TOPCon solar cells after UVID and LSIR

The TOPCon cells tested in this work were sourced from an industry partner, and all cells were manufactured in 2024 with the common device structures as shown in Fig. 1a. TOPCon cells capped in between two slides of 2 mm thick oversized glass were employed for the UVID treatment to allow the comprehensive characterisation of Si solar cells to investigate the underlying mechanism. Two sets of TOPCon solar cells were studied, including the tested cells that underwent UVID treatment and reference cells without any treatment.

As shown in Fig. 1b and Table S1, compared with the reference cell, the UVID cell lost 7.9% in PCE, 6.1% in V_{OC}, while only subtly decaying in I_{SC} and FF (1.4% and 0.53% respectively), indicating V_{OC} loss is the main degradation feature. Meanwhile, increased recombination was also revealed in the comparison of PL images of a reference cell (Fig. 1c) and a UVID cell (Fig. 1d), where the PL image of the UVID cell is clearly darker than that of the reference cell, despite being obtained under the same experimental conditions. The *I–V* and PL results suggest that the UVID might be mainly due to the degradation of interface passivation.

After a 30-min light soaking process (white LED, 1 kW m^{-2}), the performance of the UVID cell recovered to an LSIR state, remarkably close to the reference one, with only 1% loss in PCE, 1.7% loss in V_{OC} and negligible loss in I_{SC}. Clearly, the LSIR mainly results from the recovery of V_{OC}, indicating

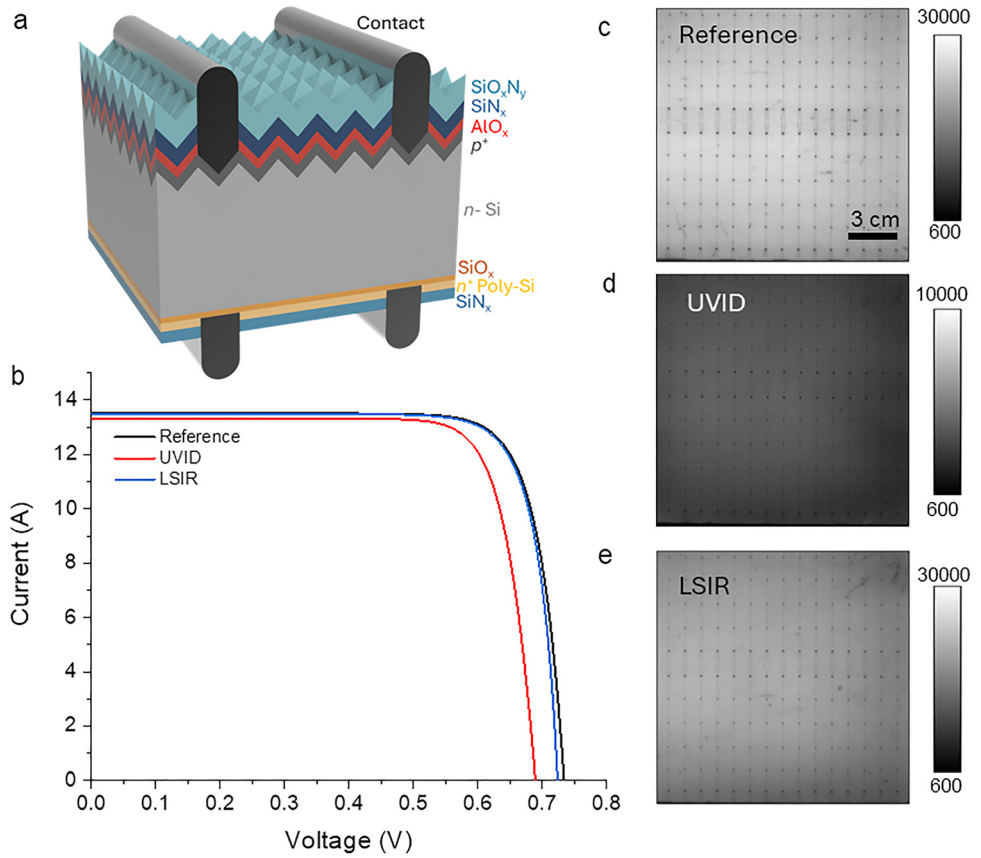

Fig. 1 *I–V* performance and PL imaging of TOPCon cells after UVID (UV60) and LSIR. (a) Schematic of the device structure of the tested cells. (b) Typical *I–V* curves of a reference cell and a UVID cell before and after LSIR. (c)–(e) PL images of the TOPCon cells in the original, UVID and LSIR states, respectively, all sharing the same length scale bar as in (c).

recovered passivation and thus reduced recombination sites. The PL image of the LSIR cell further confirms this finding with evenly enhanced PL signals (Fig. 1e) compared with the UVID cell. The recovery of cell performance after light soaking demonstrates that the UVID in TOPCon solar cells is reversible. Notably, FF can also recover after LSIR, which may result from the recovered boron doping level. The underlying mechanism will be discussed in the following two sections *via* analysing the microstructure changes of the cells during the reversible process.

Reversible changes in optical property in the UVID-LSIR cycle

UV light has been identified as a critical factor affecting the performance of ARC layers, particularly those composed of SiO_xN_y/SiN_x stacks.[7] These ARC layers are designed to minimise optical losses by reducing reflection and enhancing light absorption in the solar cell.[16] However, exposure to UV light can alter the optical properties of these layers, leading to a degradation in cell performance. The optical changes in SiO_xN_y/SiN_x ARC layers with UVID process and the subsequent LSIR process are investigated by UV-VIS reflection measurements, Fourier-transform infrared spectroscopy (FTIR) spectra, and external quantum efficiency (EQE) measurements to elucidate the mechanisms underlying these phenomena.

UV-VIS reflection measurements were conducted to evaluate the impact of UVID on the optical properties of the front surface of the cells (circled area in Fig. 2a). After UVID, a visible change in the main reflection peak at short wavelength (300 to 500 nm) was observed along with an increase in reflection within the long wavelength range of 700 to 1000 nm (Fig. 2b). Namely, the value of $n \times d$ decreases after UVID, where n and d are the refractive index and thickness of the ARC layer, respectively. Interestingly, the reflection spectra of the front surface exhibited effective recovery after light soaking. The increased long wavelength range reflection drops after LSIR and the main reflection peak at short wavelength moves back close to that of the reference cell, *i.e.*, the value of $n \times d$ re-increases after LSIR. Since the thickness of ARC layer, d, is unlikely to change remarkably or reversibly with UVID and LSIR, the refractive index might be the main reason for the change in the value of $n \times d$.

FTIR measurements were subsequently conducted on the reference, UVID, and LSIR cells to further examine this reversible trend of optical properties at the material level (Fig. 2c). Since the FTIR analysis was performed on the full cell structure, only the absorbance peak at $\sim$854 cm^{-1} (corresponding to the asymmetric Si–N stretching mode) was distinctly observed. This peak serves as an indicator of changes in the silicon nitride layer, whose intensity can be linked to the chemical

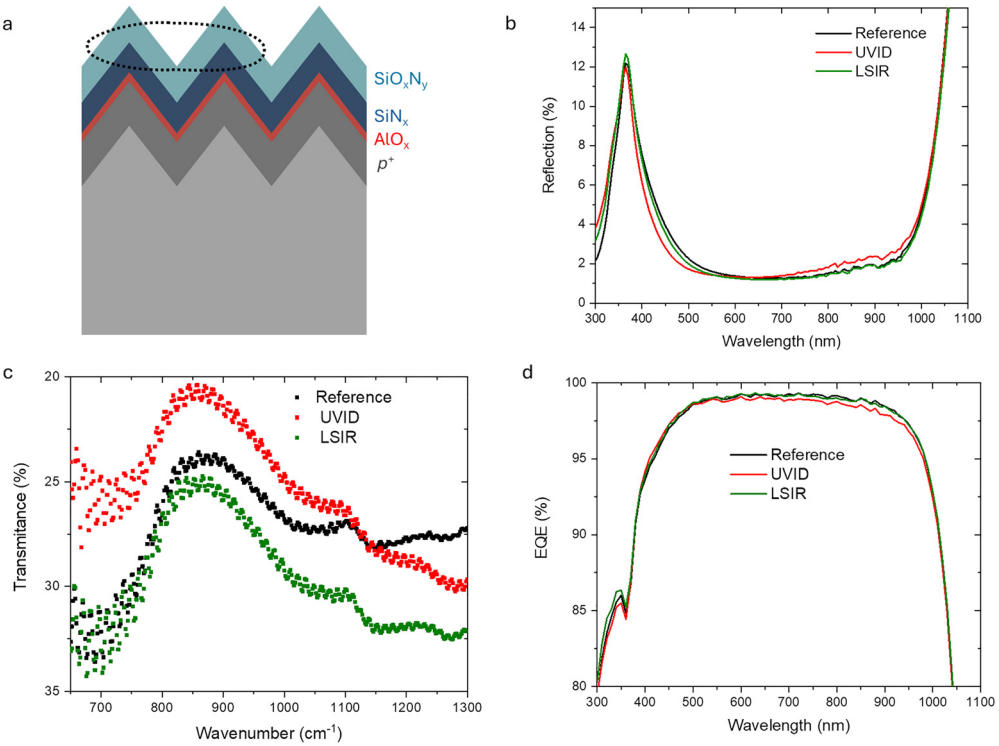

Fig. 2 The evolution of optical properties of the front surface of TOPCon cells. (a) Schematic showing the investigated region in TOPCon cells. (b) UV-VIS reflection, (c) FTIR and (d) EQE spectra of reference, UVID and LSIR cells, respectively. The curves in Fig. 2c and d were obtained from the same samples as in Fig. 2b for consistency. The FTIR measurement was taken from the cell area in between two metal fingers to avoid signals from other parts of the tested cell.

composition[17,18] of SiN_x and also its refractive index, n.[19] The Si–N absorbance peak increases after UVID whilst reducing after LSIR. This increase of the Si–N peak aligns with that reported in PERC cells after UVID, which is likely due to the breaking of Si–H and N–H bonds by UV exposure.[7] The change in Si–N bonds might indicate the alteration of the optical property of the ARC layer and therefore affecting the front surface reflection. Thus, the observed UVID-LSIR evolution in reflectance (R) might be attributed to structural and compositional alterations within the ARC layers, involving Si–N, N–H and Si–H bond reconfiguration.

To further investigate the correlation of change in R with the cell current, EQE measurement was conducted (Fig. 2d). The EQE also reveals a reversible evolution in current, which decreases from 41.19 to 41.11 mA cm^{-2} after UVID and recovers to 41.24 mA cm^{-2} after LSIR. Re-examining the reflection spectra in Fig. 2b to correlate with the EQE spectra, despite UV exposure leading to increased reflection loss in the long wavelength range of 700 to 1000 nm, it also decreases the reflection in the 400–500 nm wavelength range. However, in this short wavelength range (400–500 nm), the decreased reflection after UVID did not result in any improvement in EQE (Fig. 2d). Therefore, internal quantum efficiency (IQE) was calculated to reveal the buried change in the spectral response of the tested cell during the UVID and LSIR process. The IQE spectra (Fig. S1) clearly reveals that the main reason for the UVID-induced decrease in current lies in the considerable loss in IQE at short wavelengths (380–500 nm), which is effectively recovered after LSIR. In addition, the corresponding current values are calculated based on the spectra of EQE, IQE and reflection (Fig. S1), which also further confirms that IQE change at short wavelength is the main factor influencing the current change in the UVID and LSIR process. Since the UV-induced decrease in IQE at short wavelengths likely results from surface passivation deterioration,[20,21] the evolution of front surface passivation in UVID and LSIR is systematically investigated in the following sections.

Reversible changes in the Si top surface

Considering surface passivation is an important factor affecting both the J_{SC} (revealed by EQE & IQE), and the V_{OC} (evaluated by PL imaging) during UVID, the changes in the top surface layers were investigated by a UV Raman spectroscopy. Raman spectroscopy, particularly in the visible wavelength range, has been widely used to study Si–H bonds in HJT solar cells,[10] providing direct insights into the UVID process. However, visible Raman spectroscopy has a large absorption depth into the bulk of Si wafer, which overshadows signals from the top surface layer. In addition, direct characterisation on Si–H bonds with signature Raman (FTIR) peaks in the 1800–2300 cm^{-1} region is very challenging, as there is much less H in TOPCon cells compared with HJT cells. To overcome these limitations, we utilised 325 nm UV Raman spectroscopy, which offers a shallow penetration depth in Si (<30 nm).[22–25] Hence, the obtained UV Raman spectra are sensitive to the very top layer of the tested Si

cell, allowing us to focus on the p^+ emitter layer near the AlO_x/Si interface, as indicated by the circled area in Fig. 3a. Moreover, this non-destructive Raman characterisation (SI 3) enables efficient *in situ* monitoring of the whole UVID and LSIR processes, facilitating revelation of the mechanism.

As shown in the UV Raman spectra (Fig. 3b) collected from the top surface of TOPCon cells, the reference cell exhibited a Si Raman peak at $\sim$519.5 cm^{-1} with a full width at half maximum (FWHM) of 18 cm^{-1}. The line shape matches the characteristic of boron (B)-doped crystalline silicon, which tends to show an asymmetric Raman peak positioned at lower wavenumber than intrinsic Si.[24,26,27] After UVID, the Raman peak became narrower and shifted to a higher wavenumber, indicating a less doped, intrinsic-silicon-like structure. This trend is also verified by comparing the statistical values of peak position and FWHM calculated from a series of UV Raman spectra obtained from reference and UVID cells (Fig. 3c and d). Remarkably, light soaking reversed the change induced by UVID, restoring the Si Raman peak to its original position and width, as shown in Fig. 3b–d. This reversible change in Si Raman peak might be attributed to the variation of active B doping concentration in the top surface layer of TOPCon cells, as UV Raman spectra have been used to reveal the doping profile of B-doped Si wafers.[26]

To further validate these findings, an ultra-fast *in situ* examination protocol was developed and performed on the reference cell and LSIR recovered UVID cell (Fig. 3e, f and Fig. S2). These *in situ* measurements monitor the whole process of degradation with gradually increasing UV dose and light soaking recovery. In each *in situ* UV Raman test, the same small cell area ($\sim$22 μm in diameter, Fig. S2c–f) was repeatedly exposed to strong UV laser (325 nm, $\sim 5 \times 10^{-3}$ mW μm^{-2}) for an extended

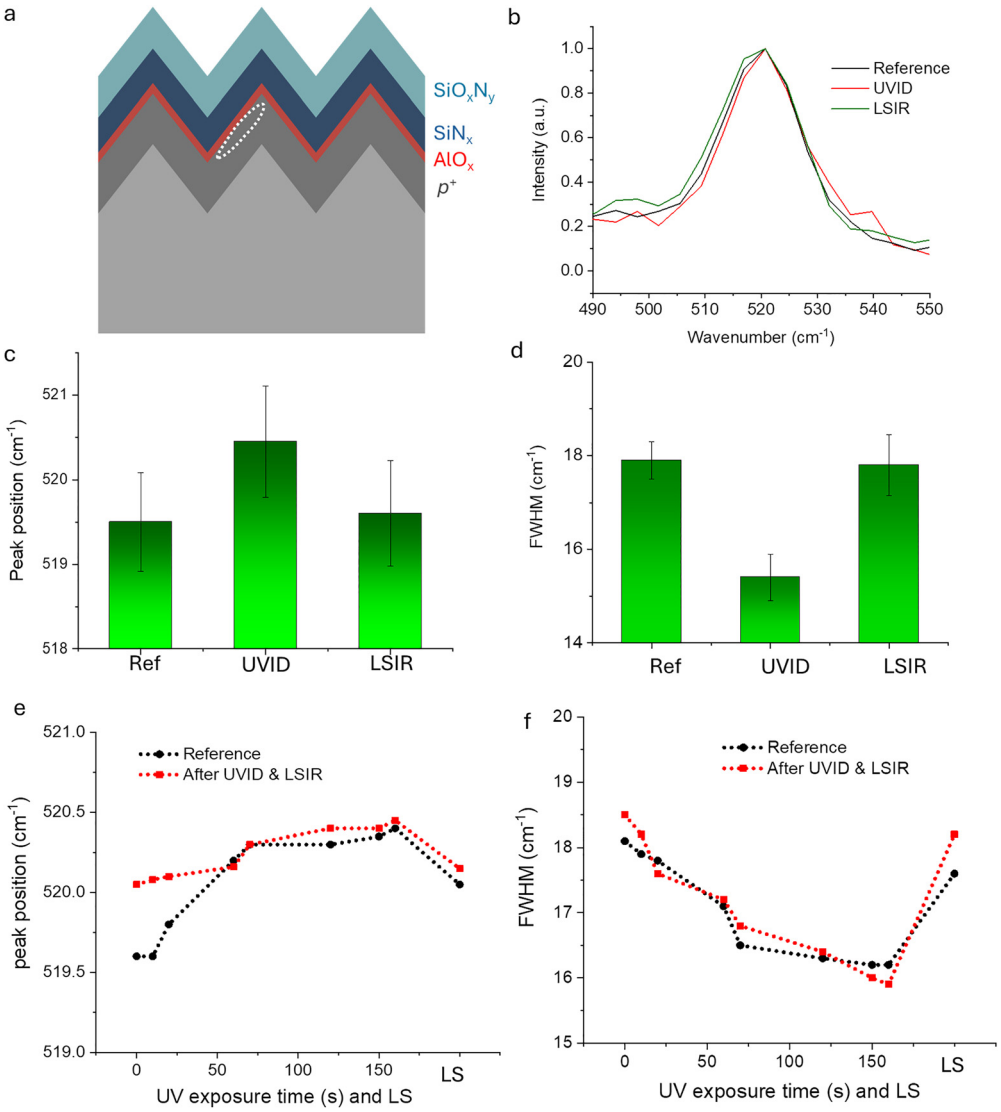

Fig. 3 The evolution of Raman spectra. (a) Schematic showing the tested region (circled area) by UV Raman. (b) Typical Raman spectra of reference, UVID and LSIR cells after normalisation to demonstrate the change in curve shape, (c) and (d) are statistical values of peak positions and FWHM for reference, UVID and LSIR cells, while (e) and (f) are the evolution trend of these two parameters during the *in situ* Raman measurement.

period, and one Raman spectrum was collected during the exposure in certain intervals with a total exposure time from 10 s to 160 s with a corresponding dose ranging from 13.9 to 222.4 kWh m^{-2}.

For the reference cell, the Si Raman peak becomes narrower and shifts to larger wavenumber with prolonged UV exposure, indicating that the higher UV dose will induce more degradation. This change is reversed after 20 minutes of following *in situ* light soaking, consistent with the observations in the aforementioned *ex situ* Raman measurements. Additionally, the cell that had undergone *ex situ* UVID and LSIR processes was also subjected to the same *in situ* Raman test. This cell shows the same degradation and recovery trend, notably with an increased degree of changes in FWHM compared to the reference cell. These two rounds of UVID and LSIR on this cell also indicate that this process can be cyclically reversed.

This *in situ* measurement further validates that the UV Raman is a non-destructive, ultra-fast and *in situ* testing method that might be suitable for potential in-line quality control. Since each Raman examination of equivalent UV 60 takes only 43 s, decent high throughput can be readily achieved in production lines. Higher testing speed is also achievable by further adjustment in laser intensity and setup optimisation.

Hypothesis of underlying mechanism for reversible UVID and LSIR

To corroborate the Raman findings and provide a deeper understanding of the UVID mechanism, atom probe tomography (APT) was performed to investigate atomic-level elemental distribution of B, H, and other relevant atoms along the top surface layers of reference and UVID cells. Based on the calibration using the Al and Si profile, the AlO_x/Si interface was identified where Al atomic ratio starts to increase from 0, and revealed by white/yellow backgrounds in Fig. 4a and b. Subsequently, cylinder shapes of examined area/volume were carefully chosen across the AlO_x/Si interfaces from the APT 3D reconstruction maps of two samples as shown in Fig. S3a. 1D concentration profile analysis of B and H were then extracted along the chosen region of interest (red cylinders) among the spatial distribution of silicon (grey) and aluminum (blue). In this manner, the UV-induced change in elemental distribution across the AlO_x/Si interface, including B and H, can be clearly revealed.

In the region below the AlO_x/Si interface (p^+ white region in Fig. 4a, also the same area probed by UV Raman spectroscopy), there is only subtle change in the B concentration in the APT profile. 3D reconstructions of B distribution in reference and UVID cells are further given in Fig. S3c and d to confirm this subtle change. Contrastingly, a much larger change in active B doping level is revealed by the significant UVID-induced FWHM change of B-doped Si Raman peak, based on the correlation between FWHM change and B-doping level that has been reported in previous paper.[26] These suggest the Si Raman peak change may be attributed to the changes in the bonding state of B that affects the active B doping concentration. One possible route is that some B atoms change from Si–B to Si–H–B, becoming inactive dopants.

As expected, more H element is found within the Si p^+ layer after UVID (Fig. 4b). The H concentration in the UVID sample was notably higher than that in the reference sample, extending to the emitter region. Our first-principles density functional theory (DFT) results indicate that, within crystalline silicon, the Si–H–B bonded configuration is more stable than the other two configurations where H and B atoms bond with Si separately (Fig. 4c). Thus, the increased H in the Si p^+ layer after UVID, prefers to form Si–H–B bonds and therefore results in a less heavily p-type doped silicon as was discovered in the Raman spectra of UVID sample.

Thus, one potential mechanism for the reversible UVID-LSIR process is proposed based on APT results and verified using Nudged Elastic Band (NEB) modelling. Under UV illumination, both Si–H and Si–B bonds are susceptible to dissociation by the high energy UV photons given that Si–H and Si–B bonds possess similar bond energies (3.0, and 3.1 eV, respectively).[28] The dissociation of Si–H at the surface will generate Si dangling bonds and free H atoms. The released H, being highly mobile due to its low atomic mass, diffuses deeper into the p^+ Si region with a lower H concentration and forms Si–H–B complexes, which partially compensate for the p-type doping, supported by the aforementioned Raman analysis. This H migration, creating Si dangling bonds, deteriorates surface passivation. As calculated in SI 5, both the reduced B doping density and damaged surface passivation lead to the decreased V_{OC} (Fig. S5), which is the main macroscopic feature of the discovered UVID effect. In addition, the initial strong upward band bending at the Si surface, established by negative fixed charges in the AlO_x layer, creates a built-in electric field that repels minority carriers and enhances field-effect passivation.[29] During UVID, the breaking of Si–H bonds and the formation of charged surface states partially neutralise these fixed charges, reducing the field strength. This flattens the energy bands near the surface, weakens carrier repulsion, increases surface recombination, also leads to a drop in V_{OC}.

Since the dissociated H is held in the subsurface region under the AlO_x/Si interface after UVID (Fig. 4a), the recovery of UVID is possible by driving H back to re-passivate the Si surface dangling bonds, which can be realised by several different driving stimuli, with LS as an effective one. In the LSIR, the high energy photons in the soaking light might break the bonding of Si–H–B,[30] releasing H. Meanwhile the B from the anti-bonded Si–H–B can re-form Si–B, which recovers the active B doping concentration under the AlO_x/Si interface as tracked in Raman spectra (Fig. 3c–f). In p^+ Si under light soaking, holes accumulate near the surface, driven by the internal electric field at the AlO_x/Si interface, thereby restoring the upward band bending. The re-established electric field can subsequently drive the H (H^+ ions) released from Si–H–B back toward the interface, enabling re-passivation of Si dangling bonds and facilitating the recovery of V_{OC}.

To verify this proposed UVID-LSIR process, a set of theoretical transition states obtained from NEB calculations are

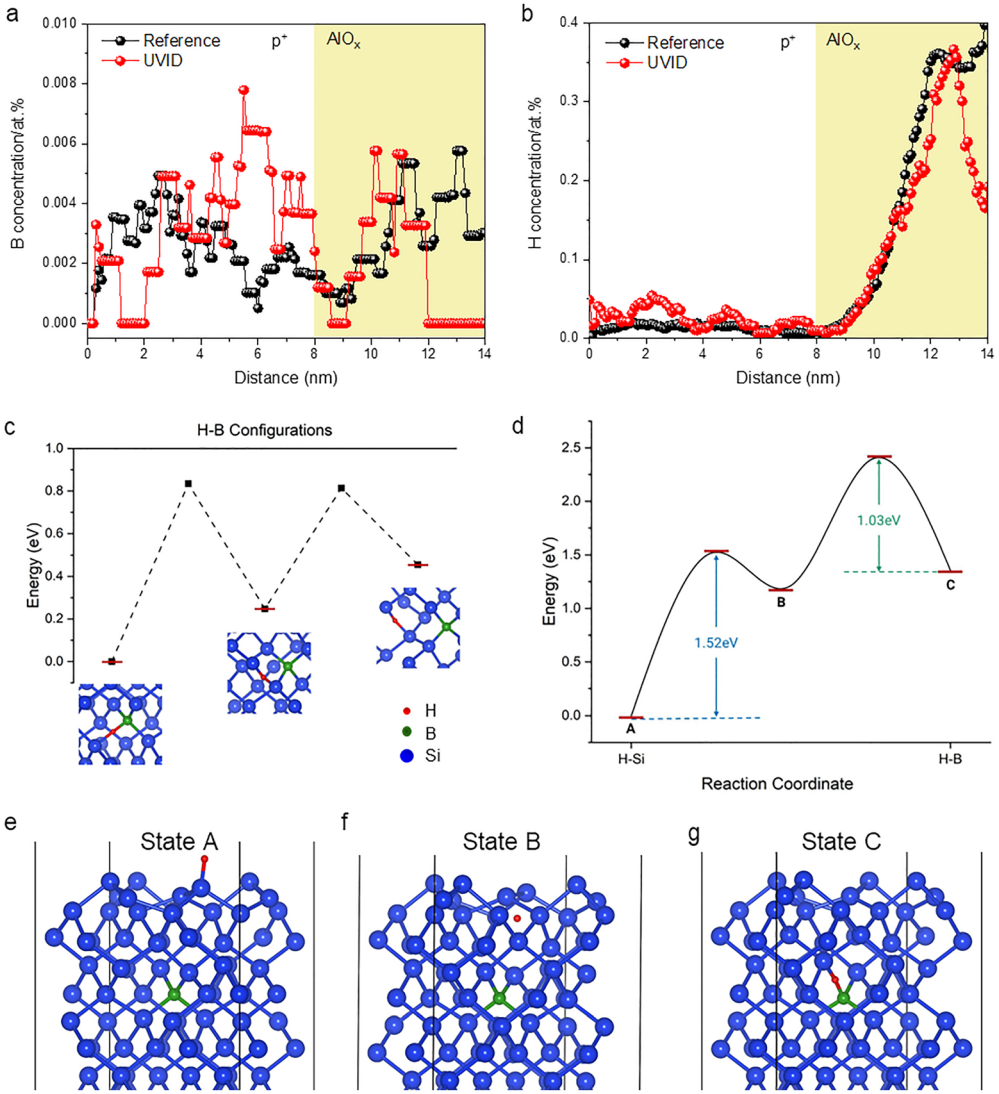

Fig. 4 1-D concentration profile of (a) B and (b) H across the interface of AlO_x and p^+ region derived from the highlighted area in Fig. S4 in reference and UVID cells (detailed in SI 4). (c) Three configurations of H–B and their relative system energies. The configuration in which H is located near the centre of the B–Si bond exhibits the lowest energy, indicating the formation of a B–H bond. (d) NEB calculation results, with states A, B and C demonstrated in (e)–(g) respectively. State A corresponds to the configuration where H passivates the Si surface by forming H–Si bonds; State B represents the intermediate state where H penetrates into the subsurface region; and State C denotes the formation of a B–H bond. The sequence A–B–C represents the UVID irradiation process, while the reverse sequence corresponds to the LSIR process.

shown in Fig. 4d–g. State A corresponds to the configuration where H passivates the Si surface by forming Si–H bonds; State B represents the intermediate state where H penetrates into the subsurface region; and State C denotes the formation of a Si–H–B bond. The A to C sequence represents the UVID irradiation process, which has an energy barrier of 1.52 eV, whereas the LSIR recovery process (C to A) exhibits a lower barrier of 1.03 eV, indicating LSIR requires a lower activation energy. The lower energy barrier for LSIR than that for UVID agrees with our experimental results and the proposed mechanism. Moreover, this difference may be underestimated as the electric field established by the negative fixed charges in the AlO_x layer that may suppress the UVID process was neglected in this simplified NEB modeling.

The mechanism analysis based on the Raman and APT results suggests a hypothesis that the UVID-LSIR process in TOPCon cells might be correlated to UV-related breakage and reformation of chemical bonds between H, B, and Si atoms. The reversibility of these changes through light soaking offers a pathway of self-recovery in field deployment where light soaking is readily available.

Examination of the high UVID-resistance TOPCon cells

The characterisation of the two identified reversibly transformable layers is further extended to the high UVID-resistance TOPCon cells to examine their material-level UV response. The results demonstrate that the UVID-resistant cells have only subtle changes in both macroscopic cell performance and

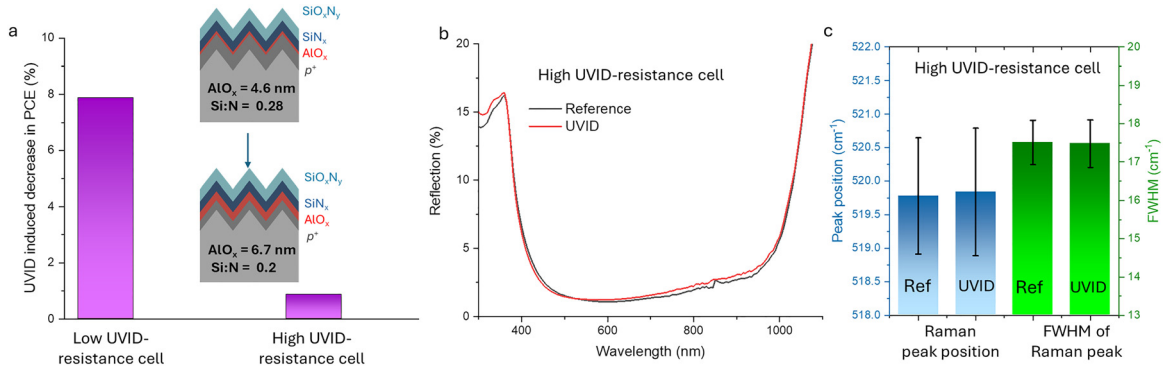

Fig. 5 Characterisation of high UVID-resistance TOPCon cell. (a) Histograms showing the decrease in PCE for high and low UVID-resistance cells, the inserts showing the differences in the device structures. (b) UV-Vis reflection spectra and (c), histograms of statistical values of Si Raman peak positions and FWHM of high UVID-resistance TOPCon cell before and after UVID.

microscopic material layers after UV radiation, suggesting that the two microscopic level material deformations identified in this work can reflect the main degradation mechanism and can act as a good indicator of the UVID resistance of TOPCon cells.

The high UVID-resistance is achieved through two strategies, increasing the thickness of AlO_x from 4.6 to 6.7 nm and reducing the Si/N ratio of SiN_x ARC layer from 0.28 to 0.2. The increase of AlO_x thickness is reported to suppress the UV-induced efficiency loss of TOPCon solar cells.[8] The thicker AlO_x could mitigate the UV-induced degradation process identified in our proposed mechanism by maintaining the H passivation at the AlO_x/Si interface during UVID. On the other hand, the reduced Si/N ratio also increases the reflection at the UV region to reduce the impact of UV radiation, according to previous study[31] and our simulations (Fig. S6).

As shown in Fig. 5a, the high UVID-resistance cell has less than 1% degradation in PCE after UV60 treatment, compared with the 8% PCE degradation in the aforementioned low UVID-resistance cell that underwent the same UV treatment. At the material level, the front surface reflection (Fig. 5b) of the high UVID-resistance cell shows a similar trend of change in the main peak at short wavelengths and an increased reflection at long wavelengths after UVID, but with much less amplitude of change in the value of $n \times d$ after UVID compared to the low UVID-resistance cell (Fig. 2b). Similar results are observed in the UV Raman measurements as well. The Si Raman peak of high UVID-resistance cell tends to move towards the intrinsic Si spectrum with peak position at larger wavenumber and narrower width (Fig. 5c) after UVID, but the change is very subtle compared with that in the low UVID-resistance cell (Fig. 3c and d). These findings validate that the above microscopic level characterisations may be used to examine the effectiveness of high UVID-resistance strategies.

Finally, the absolute PCE of high and low UVID-resistance cells can be compared to further emphasise the importance of understanding this reversible UVID process. To fabricate high UVID-resistance cells, thicker AlO_x layer and adjusted Si/N ratio are used, leading to slightly decreased cell performance of 23.52% PCE (which barely decays with UV60) compared to 24.03% initial PCE of the low UVID-resistance cell (which decays to 22.14% after UV60 and recovers to 23.86% after LSIR). Despite being influenced by UVID, the LSIR recovered low UVID-resistance cell still has higher PCE than the high UVID-resistance cell, indicating the real performance of the low UVID-resistance cell in the field might be better. This highlights the importance of understanding the mechanism of reversible UVID to avoid this loss in performance and high production cost of fabricating thicker AlO_x layer.

Conclusion

In this work, we developed a non-destructive material-level characterisation platform to investigate the reversible UVID mechanism of TOPCon solar cells. Two reversible changes were revealed in the front surface ARC layer and the top surface Si layer during the UVID and LSIR processes. The correlation of the macroscopic cell performance change with the two reversible changes at the material level provides important insight into the mechanism of this reversible UVID process. One reasonable hypothesis proposed based on Raman and APT results is that this process is due to the breakage and reformation of chemical bonds between H, B and Si atoms under UV and light soaking, affecting the cell passivation as well as boron-doping, which is also supported by theoretical modelling. Furthermore, we demonstrate that the use of a thicker AlO_x film and lower Si:N ratio SiN_x layer can increase UVID-resistance of TOPCon cells, which is confirmed by the material-level characterisation. In addition, the developed non-destructive, ultra-fast, *in situ* Raman-based examination can be used as an effective diagnosis tool and quickly assess the UVID resistance of tested TOPCon cells, which can be potentially integrated into manufacturing workflows for in-line quality control in the future.

Methods & protocols

Materials

The tested TOPCon cells in this work were sourced from the industry partner, in which the SiN_x layer is deposited by PECVD

with a stoichiometry of NH_3/SiH_4 = 0.28 and the AlO_x is deposited by ALD with the thickness of 4.6 nm. All cells were manufactured in 2024. The received cells are 183 mm × 182 mm in size. The cells were cut into smaller suitable sizes to carry out UV-Vis, EQE, FTIR, Raman and APT measurements.

UVID & LSIR treatments

UVID treatment: The initial UVID treatment of UVID cells was carried out with a HONLE SUV10000T chamber installing HONLE UV 2000F UV LEDS. The light source used contains 5% UVB according to IEC 61215 standards. The TOPCon cells were first sandwiched in between two oversized 2 mm thick glass slides with edges covered by aluminium foil and then exposed to 140 W m^{-2} UV light at 60 °C with a total UV exposure dose of 60 kWh m^{-2}. To achieve UV60, an exposure time of ~430 h is needed. While for the 325 nm laser used for Raman measurement, the laser intensity is ~5 × 10^{-3} mW μm^{-2} = 5 × 10^9 mW m^{-2} = 5000 kW m^{-2}. To achieve UV 60, only ~43 s is needed.

LSIR treatment: The light soaking was carried out in a Solstice LED light soaker box where the TOPCon cells undergone a 30 min light exposure process (white LED, 1 kW m^{-2}). In our *in situ* Raman test, the camera-integrated focusing beam (white LED light source) for observing the sample is used *in situ* for LSIR, which can also effectively recover UVID in 30 min.

Characterisation

The following characterisations were performed at UNSW's solar cell characterisation lab and Mark Wainwright Analytical Centre. *I–V* performance of the TOPCon cells was examined using a PVTools LOANA cell tester, and PL images were recorded using a BT Imaging LIS-R1 PL imager under the same exposure time and laser intensity. UV-Vis reflection spectra were collected using a PerkinElmer Lambda 1050 spectrophotometer. To obtain consistent results, small masks were used to avoid the thick bus bars on the TOPCon cells. The curves in Fig. 2b were obtained in the same testing session to avoid unnecessary errors from instrument calibration. EQE measurements were performed using a PV Measurements QEX7 Spectral Response setup. The tested areas are carefully chosen to exclude any thick bus bars during each test. FTIR measurements were carried out by a Spectrum 3 FIR/Spotlight 400 FTIR spectrometer. The tested areas are carefully chosen to exclude any thick bus bars during each test. Raman spectra and mapping were recorded using an inVia Qontor Raman spectrometer combined with laser sources of different wavelengths was employed for UV Raman spectra, achieving absolute spectroscopic resolution of 1.2 to 3.8 cm^{-1} based on the selection of laser wavelength and gratings. To achieve strong Raman signals from Si cells with 325 nm UV laser for subsequent theoretical fitting, 325 nm UV laser is combined with 2400 l cm^{-1} grating to achieve spectroscopic resolution of 3.8 cm^{-1}. Calibration was carried out before every UV Raman test using standard diamond sample and polished intrinsic Si wafer sample, and the Raman peak of intrinsic Si is set to 520.5 cm^{-1} in every calibration. The tested areas are carefully chosen in the middle of two metal fingers on the surface of TOPCon cells. All the Raman curves were taken using the same measurement condition for comparison purposes. The peak position and peak width of obtained Raman curves are subsequently calculated by fitting the obtained Raman curves with built-in equations in the "WiRE 5.6" software. The same Raman setup was also employed to carry out *in situ* UV exposure and light soaking treatment. To realise the *in situ* UV Raman monitoring (Fig. 3e and f), the *in situ* UV exposure was carried out by the 325 nm UV laser incorporated in the Raman spectrometer. While the *in situ* light soaking was carried out by exposing the tested area to the focusing beam used in the Raman microscope. APT needle specimens were lifted out in a focused-ion beam/scanning electron microscope (Helios G4 PFIB UXe). APT needle specimens were analysed on the Invizo 6000 at 50 K using dual laser-pulsed mode with 400 pJ laser pulse energy and a pulse rate of 200 kHz. APT data analysis was performed in the commercial software APSuite (Version 6.3., CAMECA).

Modelling

First-principles DFT calculations were performed using the Vienna *Ab Initio* Simulation Package (VASP).[32,33] The exchange–correlation interactions were described within the generalised gradient approximation (GGA) using the Perdew–Burke–Ernzerhof (PBE) functional.[34] A Si(001) surface slab containing 72 atoms was constructed, and a single B atom was introduced to investigate the interactions among Si, B, and H atoms. The Si(001) surface undergoes the characteristic (2 × 1) dimer reconstruction, which reduces surface energy by pairing adjacent Si atoms.[35] After testing multiple adsorption configurations, the adsorption site of H on the Si(001) reconstructed surface was selected based on the lowest total energy. The energy barriers were calculated using the NEB method.[36] During the geometry optimisation, atomic positions were fully relaxed until the forces on all atoms were smaller than 0.01 eV $Å^{-1}$ and total energy change was smaller than 1 × 10^{-7} eV. The Brillouin zone was sampled at the Γ-point with a 3 × 3 × 1 *k*-point mesh. All structure illustrations were performed using VESTA.[37]

Author contributions

X. H., Z. L., C. L. and P. Z. conceived the project. X. H. and Z. L. supervised the project. P. Z., C. L., and Z. L. designed the experiments and conducted the characterisations. K. Y., J. Z., L. M., J. Z, T. L., J. Y. W. T. X. Z. and H. J. provided the TOPCon cells and carried out UVID tests. J. H. and J. C. conducted the APT measurements. J. C., M. S. and J. Z. L. caried out the theoretical modelling. S. W. contributed to the discussion of the UVID mechanism. P. Z., C. L. and Z. L. drafted the paper. All authors contributed to the final manuscript.

Conflicts of interest

There are no conflicts to declare.

Data availability

The data supporting this article have been included as part of the supplementary information (SI). Supplementary information is available. See DOI: https://doi.org/10.1039/d5ee05078b.

The code for the VTST (VASP Transition State Tools) package used in this study can be found at https://theory.cm.utexas.edu/vtsttools/ with DOI – https://doi.org/10.1063/1.1329672, maintained by the Henkelman group. The version of the code employed for this study is version 4.1.

Acknowledgements

This work was supported by the Australian Research Council Research Hub for Photovoltaic Solar Panel Recycling and Sustainability (PVRS). M. G. acknowledges financial support by the Australian Centre for Advanced Photovoltaics. Responsibility for the views, information or advice expressed herein is not accepted by the Australian Government. The authors acknowledge the use of facilities and the scientific and technical assistance at the Electron Microscope Unit, Solid State & Elemental Analysis Unit, and Spectroscopy Laboratory within the Mark Wainwright Analytical Centre (MWAC) at UNSW Sydney. The authors acknowledge the facilities, and the scientific and technical assistance, of the Australian Microscopy and Microanalysis Research Facility at the Australian Centre for Microscopy and Microanalysis at the University of Sydney. The authors acknowledge the use of computational resources from the UNSW Resource Allocation Scheme on the National Computational Infrastructure (NCI) high performance computing system, Australia, under DOI: https://doi.org/10.26190/PMN5-7J50.

References

1 L. Yang, Z. Hu, Q. He, Z. Liu, Y. Zeng, L. Yang, X. Yu and D. Yang, *Sol. Energy Mater. Sol. Cells*, 2024, **275**, 113022.
2 J. Yang, Y. Tang, C. Zhou, S. Chen, S. Cheng, L. Wang, S. Zhou, X. Jia, W. Wang, X. Xu, J. Xiao and W. Wei, *Sol. Energy Mater. Sol. Cells*, 2024, **276**, 113062.
3 P. Gebhardt, U. Kräling, E. Fokuhl, I. Hädrich and D. Philipp, *Progress in Photovoltaics: Research and Applications*, 2024.
4 W. Xu, P. Zhou, Q. Xiu and X. Xing, *AIP Adv.*, 2025, **15**, 025010.
5 F. T. Thome, P. Meßmer, S. Mack, E. Schnabel, F. Schindler, W. Kwapil and M. C. Schubert, *Sol. RRL*, 2024, **8**, 2400628.
6 H. Ye, S. Huang, C. Qian, Z. Sun, Y. Chen, X. Song, Y. Zhang, N. Wang, Y. Hu, Y. Yang, L. Li, Z. Ma, T. Chen, W. Liu and J. Yu, *Sol. RRL*, 2023, **7**, 2300334.
7 S. Huang, Y. Ma, L. Li, J. Tu, J. Yu, L. Lei, H. Luo, Y. He, J. Hou, L. Kong and L. Xiao, *Sol. Energy Mater. Sol. Cells*, 2025, **289**, 113693.
8 Z. Li, K. Yu, Q. Zhu, L. Wang, Y. Chen, J. Huang, G. Zhou, X. Sun, J. Gao and L. Zhou, *Sol. Energy Mater. Sol. Cells*, 2025, **289**, 113691.
9 A. Sinha, J. Qian, S. L. Moffitt, K. Hurst, K. Terwilliger, D. C. Miller, L. T. Schelhas and P. Hacke, *Prog. Photovoltaics Res. Appl.*, 2023, **31**, 36–51.
10 B. Fischer, A. Lambertz, M. Nuys, W. Beyer, W. Duan, K. Bittkau, K. Ding and U. Rau, *Adv. Mater.*, 2023, **35**, 2306351.
11 N. Wang, F. Meng, L. Zhang, Z. Liu and W. Liu, *Carbon Neutrality*, 2024, **3**, 18.
12 International Technology Roadmap for Photovoltaic (ITRPV), 2025.
13 B. Hoex, J. Schmidt, P. Pohl, M. C. M. van de Sanden and W. M. M. Kessels, *J. Appl. Phys.*, 2008, **104**, 044903.
14 L. E. Black, T. Allen, K. R. McIntosh and A. Cuevas, *J. Appl. Phys.*, 2014, **115**, 093707.
15 B. Veith-Wolf, R. Witteck, A. Morlier, H. Schulte-Huxel and J. Schmidt, Effect of UV illumination on the passivation quality of AlOx/c-Si interfaces, 2016 IEEE 43rd Photovoltaic Specialists Conference (PVSC), Portland, OR, USA, 2016, pp. 1173–1178, DOI: 10.1109/PVSC.2016.7749799.
16 S. M. F. Zhang, A. Gentle, M. Bilokur, N. Song, Z. Yang, Y. Jiang, H. Teasdale, R. Bhoopathy, I. Perez-Wurfl and Z. Hameiri, *Sol. Energy Mater. Sol. Cells*, 2025, **282**, 113389.
17 K. O. Bugaev, A. A. Zelenina and V. A. Volodin, *Int. J. Spectrosc.*, 2012, **2012**, 281851.
18 S. Jafari, J. Hirsch, D. Lausch, M. John, N. Bernhard and S. Meyer, *AIP Conf. Proc.*, 2019, **2147**, 050004.
19 Alamgeer, H. Yousuf, R. U. Rahman, S. Jang, S. Rehan, M. Q. Khokhar, S. Park and J. Yi, *Mater. Sci. Semicond. Process.*, 2025, **192**, 109483.
20 B. Mojrová, H. Chu, C. Peter, P. Preis, J. Lossen, V. D. Mihailetchi and R. Kopecek, *Energy Procedia*, 2017, **124**, 288–294.
21 A. K. Sharma, S. K. Agarwal and S. N. Singh, *Sol. Energy Mater. Sol. Cells*, 2007, **91**, 1515–1520.
22 R. Liu and M. Canonico, *AIP Conf. Proc.*, 2003, **683**, 738–743.
23 D. Pastor, J. Olea, A. del Prado, E. García-Hemme, I. Mártil, G. González-Díaz, J. Ibáñez, R. Cuscó and L. Artús, *Semicond. Sci. Technol.*, 2011, **26**, 115003.
24 S. Palleschi, D. Mastrippolito, P. Benassi, M. Nardone and L. Ottaviano, *Appl. Surf. Sci.*, 2021, **561**, 149691.
25 M. Kadlečíková, Ľ. Vančo, J. Breza, M. Mikolášek, K. Hušeková, K. Fröhlich, P. Procel, M. Zeman and O. Isabella, *Optik*, 2022, **257**, 168869.
26 D. Mastrippolito, S. Palleschi, S. Tosti and L. Ottaviano, *Appl. Surf. Sci.*, 2021, **567**, 150824.
27 B. G. Burke, J. Chan, K. A. Williams, Z. Wu, A. A. Puretzky and D. B. Geohegan, *J. Raman Spectrosc.*, 2010, **41**, 1759–1764.
28 Webelement, 2025.
29 X. Niu, S. McNab and R. S. Bonilla, *APL Electronic Devices*, 2025, **1**, 026111.
30 K. J. Chang and D. J. Chadi, *Phys. Rev. Lett.*, 1988, **60**, 1422–1425.
31 S. Duttagupta, F. Ma, B. Hoex, T. Mueller and A. G. Aberle, *Energy Procedia*, 2012, **15**, 78–83.

32 W. Kohn and L. J. Sham, *Phys. Rev.*, 1965, **140**, A1133–A1138.
33 G. Kresse and D. Joubert, *Phys. Rev. B*, 1999, **59**, 1758–1775.
34 J. P. Perdew, J. A. Chevary, S. H. Vosko, K. A. Jackson, M. R. Pederson, D. J. Singh and C. Fiolhais, *Phys. Rev. B*, 1992, **46**, 6671–6687.
35 C. J. Först, P. E. Blöchl and K. Schwarz, *Comput. Mater. Sci.*, 2003, **27**, 70–74.
36 G. Henkelman and H. Jónsson, *J. Chem. Phys.*, 2000, **113**, 9978–9985.
37 K. Momma and F. Izumi, *J. Appl. Crystallogr.*, 2011, **44**, 1272–1276.